Transcranial direct current stimulation changes resting state functional connectivity: A large-scale brain network modeling study

Tim Kunze [a,b,*], Alexander Hunold [a], Jens Haueisen [a,c], Viktor Jirsa [d,e,f], Andreas Spiegler [d,e,**]

[a] Institute of Biomedical Engineering and Informatics, Ilmenau University of Technology, Gustav-Kirchhoff Str. 2, 98693 Ilmenau, Germany
[b] Max Planck Institute for Human Cognitive and Brain Sciences, Stephanstrasse 1a, 04103 Leipzig, Germany
[c] Biomagnetic Center, Department of Neurology, University Hospital Jena, Erlanger Allee 101, 07747 Jena, Germany
[d] Aix-Marseille Université, Institut de Neurosciences des Systèmes, Marseille, France
[e] Institut de la Santé et de la Recherche Médical, UMR_S 1106, 27 Bd Jean Moulin, 13385, Marseille Cedex 5, France
[f] Centre National de la Recherche Scientifique, France

ARTICLE INFO

ABSTRACT

Transcranial direct current stimulation (tDCS) is a noninvasive technique for affecting brain dynamics with promising application in the clinical therapy of neurological and psychiatric disorders such as Parkinson's disease, Alzheimer's disease, depression, and schizophrenia. Resting state dynamics increasingly play a role in the assessment of connectivity-based pathologies such as Alzheimer's and schizophrenia. We systematically applied tDCS in a large-scale network model of 74 cerebral areas, investigating the spatiotemporal changes in dynamic states as a function of structural connectivity changes. Structural connectivity was defined by the human connectome. The main findings of this study are fourfold: Firstly, we found a tDCS-induced increase in functional connectivity among cerebral areas and among EEG sensors, where the latter reproduced empirical findings of other researchers. Secondly, the analysis of the network dynamics suggested synchronization to be the main mechanism of the observed effects. Thirdly, we found that tDCS sharpens and shifts the frequency distribution of scalp EEG sensors slightly towards higher frequencies. Fourthly, new dynamic states emerged through interacting areas in the network compared to the dynamics of an isolated area. The findings propose synchronization as a key mechanism underlying the changes in the spatiotemporal pattern formation due to tDCS. Our work supports the notion that noninvasive brain stimulation is able to bias brain dynamics by affecting the competitive interplay of functional subnetworks.

© 2016 The Authors. Published by Elsevier Inc. This is an open access article under the CC BY-NC-ND license (http://creativecommons.org/licenses/by-nc-nd/4.0/).

Introduction

Transcranial Direct Current Stimulation (tDCS) is a noninvasive technique used to affect the brain's processing by sustaining a direct current flow of up to 2 mA between scalp electrodes for a few of minutes (Brunoni et al., 2012; Dayan et al., 2013; Nitsche et al., 2008; Nitsche and Paulus, 2000; Wagner et al., 2007). Several studies report effects of tDCS on cognitive brain processes (Boggio et al., 2009) and find positive therapeutic effects on neurological and psychiatric disorders, such as rehabilitation after stroke or traumatic brain injury (Gomez Palacio Schjetnan et al., 2013; Hummel and Cohen, 2005; Lindenberg et al.,

2010), depression (Nitsche et al., 2009), and pain (Antal et al., 2010; Bachmann et al., 2010; O'Connell et al., 2014; Valle et al., 2009; Zaghi et al., 2009). These therapeutic effects have been attributed to long-term alterations of NMDA receptor efficacy due to tDCS (Liebetanz et al., 2002). Brain dynamics during or shortly after tDCS (short-term effects) show an increased excitability in response to anodal stimulation and a decreased excitability in response to cathodal stimulation (Ardolino et al., 2005; Dieckhofer et al., 2006; Jacobson et al., 2012; Lang et al., 2004; Matsunaga et al., 2004). Bindman and colleagues report on a shifting of resting state potentials and an increased rate of spontaneously triggered action potentials in vitro (Bindman et al., 1964). The short-term effects of tDCS have been quantified by power changes in resting state activity in the scalp Electroencephalogram (EEG) during tDCS (Mangia et al., 2014) and immediately after tDCS (Ardolino et al., 2005; Polania et al., 2011a; Spitoni et al., 2013). The alpha-band (8–13 Hz) shows increased power in the vicinity of an anodal tDCS site and modulations in distant electrodes (Mangia et al., 2014; Spitoni et al., 2013). tDCS transiently and reversibly changes the cortical activity elicited by visual stimulation (Antal et al., 2004). Our

* Correspondence to: T. Kunze, Max Planck Institute for Human Cognitive and Brain Sciences, Stephanstrasse 1a, 04103 Leipzig, Germany.
** Correspondence to: A. Spiegler, Institut de la Santé et de la Recherche Médical, UMR_S 1106, 27 Bd Jean Moulin, 13385, Marseille Cedex 5, France.
E-mail addresses: tim-kunze@tu-ilmenau.de (T. Kunze), andreas.spiegler@univ-amu.fr (A. Spiegler).

computational studies relate directly to the empirical findings of Polania et al. (2011a), who showed that functional connectivity following tDCS at rest increases among EEG sensors close to the cathode. This result suggests a functional reorganization and the ability to bias cortical networks. Given that various brain diseases exhibit a characteristic change in the brain's functional connectivity (Zhang and Raichle, 2010), a coordinated stimulation of the brain holds great potential to complement and enhance pertinent strategies of clinical therapy.

Computational models have been used recently to investigate the mechanisms initiated by tDCS. The local tDCS effects on experimentally observed evoked potentials (of a rabbits' somatosensory cortex in response to air-puffs applied on the whiskers) could be reproduced using a Jansen-Rit-like neural mass model (Jansen and Rit, 1995) where the stimulation perturbs the membrane potential of neurons (Molaee-Ardekani et al., 2013). To investigate changes in EEG's rhythms, this local model has been extended by Merlet and colleagues to a full brain setup of 66 uncoupled cerebral areas, each driven by an additional thalamic area and selectively affected by transcranial alternating current stimulation (tACS) through a biophysical forward calculation (Merlet et al., 2013). Merlet and colleagues report a significant increase in alpha power at posterior midline scalp electrodes due to tACS with frequencies from 8 to 12 Hz. However, Merlet and colleagues could not succeed in generating realistic scalp topographies due to the lack of long-range cortico-cortical connections (Merlet et al., 2013).

In this study, we stress the importance of structural connectivity of the brain in the spatiotemporal pattern formation influenced by tDCS. The pipeline of this study is depicted in Fig. 1. We used the structural connectivity given by the connectivity matrix of the human connectome, which represents myelinated nerve fiber bundles, to determine the coupling strengths among 74 cerebral areas. A single Jansen-Rit model described the activity of each cerebral area in terms of the mean activity of (i) pyramidal cells, (ii) excitatory interneurons, and (iii) inhibitory interneurons. The strength of tDCS on each cerebral area is obtained by a forward calculation using a high-resolution finite element head model, where the anode is placed over the left motor area and the cathode over the right frontal orbit. The mean postsynaptic potentials (PSPs) of the pyramidal cells are projected onto 62 scalp EEG electrodes using a lead field from a boundary element head model. Significant functional connectivity and frequency components are analyzed both in source and sensor space. The pattern formation is systematically investigated under rest (unperturbed) and tDCS (perturbed) dependent on the scaling of structural connectivity and tDCS. Here, we reproduced the short-time effects of tDCS in the alpha-band and demonstrated that tDCS increases the functional connectivity through synchronization.

Furthermore, we create a catalog of large-scale brain dynamics under rest and tDCS. In order to characterize an area's dynamic state, we compared the dynamics with the repertoire of an isolated area (bifurcation diagram of the local Jansen-Rit model) dependent on the dynamic network state under rest condition. In this way, we explain the network state transitions and underlying mechanisms. We find that a transition point inherent in an isolated Jansen-Rit model (i.e., bifurcation) gets spread through the interacting areas in the network, resulting in a stepwise network state transition. In addition to such cases in which network states (and transitions) can be traced back to the isolated local model, the network also introduces qualitative new dynamics through point-like transitions (with respect to the scaling of the structural connectivity) that simply cannot be traced back to the area's dynamic repertoire.
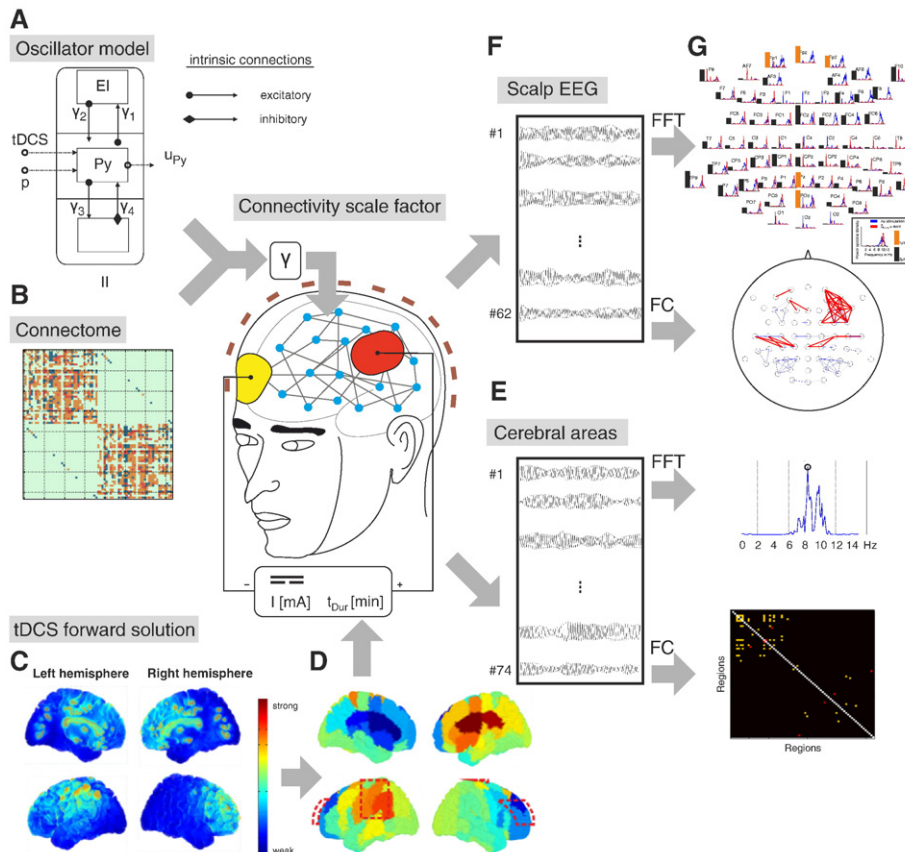

Fig. 1. Analyzing the large-scale brain network model during rest and tDCS. A set of 74 cerebral areas, each described by a Jansen and Rit model, as in panel **A**, were linked to a network according to a given connectome, as in panel **B**. The heterogeneous connectivity matrix was globally scaled by a connectivity scale factor γ. tDCS strength in the cerebral areas was determined by the current density distribution from a forward calculation, as in panel **C**. Consequently, an individual constant potential was added to each area during tDCS, as in panel **D**. The mean membrane potential of pyramidal cells in each area served as output signal, as in panel **E**, and were projected onto the 62 scalp EEG electrodes, as in panel **F**. For both data sets the frequency spectra and the functional connectivity were computed, as in panel **G**, and compared during rest and tDCS.

Materials and methods

Model architecture

Large-scale brain network model

Here we use a brain network model comprising 74 cerebral areas, each modeled by an oscillator model, which accounted for the interaction of the participating neural subpopulations (i.e., neural masses) in one area according to mean field theory (Deco et al., 2008). Following (Spiegler and Jirsa, 2013), the respective set Φ of the $n = 2$ state variables, $\Phi = [\varphi_1, \varphi_2]$, namely the mean membrane potential and mean firing rate, of each neural mass formed a vector $\Psi = [\Phi_1; \Phi_2; \ldots; \Phi_m]$ describing the state variables of a network of $m = 3$ neural masses, namely excitatory and inhibitory interneurons as well as pyramidal cells. The neural masses were interconnected according to a local connectivity matrix, $\mathbf{V}_{loc}$, which describes whether the neural masses in a neural population either act excitatory or inhibitory on each other. By interconnecting $l = 74$ of such neural mass models (each representing a single cortical area) according to a heterogeneous connectivity matrix, $\mathbf{W}_{het}$, the state variable vector of the resulting brain network model is $\Omega = [\Psi_1; \Psi_2; \ldots; \Psi_l]$. The heterogeneous connectivity matrix, $\mathbf{W}_{het}$, thus describes connectivity between all considered elements of the network (i.e., cortical areas) and is well known as the connectome. Eventually, the temporal evolution of the brain network model was described by applying a temporal differential operator $P(\mathrm{d}/\mathrm{d}t)$ to Ω as in:

$$P\left(\frac{\mathrm{d}}{\mathrm{d}t}\right) \Omega(t) = S(\mathbf{V}_{loc}\,\Omega(t)) + \Xi + \gamma\,\mathbf{W}_{het} S(\mathbf{V}_{loc}\,\Omega(t)), \tag{1}$$

with the transfer function $S(\cdot)$ and an extrinsic input Ξ. The third term on the right hand side of (1) described the links among network nodes and was globally scaled by the connectivity scaling factor, γ, which can be interpreted as a global synaptic gain signifying a neurobiological parameter, such as global axon density or a chemical substance which acts on the efficacy of synaptic connections.

Structural layout: the connectome

We used a connectome for the structural layout of the brain network model, which is included in the neuroinformatics platform *The Virtual Brain* (TVB) (Sanz-Leon et al., 2015; Sanz Leon et al., 2013). This particular connectome considered 37 cerebral areas for each hemisphere, as listed in Table 1, resulting in a total number of $N = 74$ cortical areas. The area parcellation was a hybrid based on diffusion spectrum imaging data and data from the CoCoMac neuroinformatics database (Kotter, 2004). The connectivity matrix (Fig. S1A) weights each link with 0, 1,

2, or 3 for being absent, weak, moderate, or strong, respectively. To put these gradations in relation to the topology of the structural connectivity matrix and to ensure the dissipation of activity in the network, we normalized the connectivity matrix to a unity maximum in-strength. For this each connectivity weight was divided by the maximum existing in-strength of the considered areas.

Temporal dynamics of an area: the Jansen-Rit model

The temporal dynamics of each of the 74 cortical areas were modeled through an isolated Jansen-Rit model in its original parameterization (Jansen and Rit, 1995) with the ability to oscillate within the alpha-band (8−12 Hz). All 74 cortical areas (i.e., network nodes) featured the same standard parameterization. The Jansen-Rit model comprises three neural masses, which are representative for the cerebral cortex, namely: excitatory and inhibitory interneurons and pyramidal cells. Each neural mass was described by its key state variables: the mean membrane potential $u(t)$ and the mean firing rate $m(t)$ as well as their respective mutual transformations (Jansen and Rit, 1995): a pulse-to-wave transformation via a convolution of $m(t)$ with a convolution kernel $h_{e,i}(t)$, where index e indicates excitatory processes and index i indicates inhibitory processes, and a wave-to-pulse transformation. The pulse-to-wave transformation describes the occurring processes at the dendrites, where an incoming pulse of action potentials leads to an altered membrane potential of the postsynaptic cell as in:

$$u(t) = \int_0^\infty \mathrm{d}\tau\, m(\tau) \cdot h_{e,i}(t-\tau), \tag{2}$$

where $h_{e,i}(t)$ is the impulse response and is defined as.

$$h_{e,i}(t) = \frac{H_{e,i}}{\tau_{e,i}} \cdot t \cdot \exp\left(-\frac{t}{\tau_{e,i}}\right), \quad t \geq 0, \tag{3}$$

where $H_{e,i}$ is the maximum postsynaptic potential and $\tau_{e,i}$ is a lumped representation of delays occurring during the synaptic transmission. The wave-to-pulse transformation is defined by a sigmoid function as in:

$$S(u(t)) = \frac{2e_0}{1 + \exp(r(\nu_0 - u(t)))}, \tag{4}$$

where e_0 is the maximum pulse, r is the steepness of the sigmoid function, and ν_0 is the postsynaptic potential for which half of the maximum pulse rate is achieved. This sigmoid function constituted the transfer function from Eq. (1). Thus, the temporal differential operator read:

$$P : D_i(\lambda) = \lambda^2 + 2b_i\lambda + b_i^2, \tag{5}$$

with $b_1 = b_2 = 1$ and $b_3 = 1/2$ for the pyramidal cells ($i = 1$), the excitatory ($i = 2$), and inhibitory interneurons ($i = 3$). Based on the intrinsic feedback circuitry among the neural masses (see Fig. S2), the Jansen-Rit model has a rich dynamic repertoire, which was extensively described by Spiegler and colleagues (Spiegler et al., 2010). Fig. 3A depicts a reduced version of the bifurcation diagram. Four qualitatively different dynamic states were distinguishable by means of the occurring frequency of the oscillation and the baseline of the mean PSP of the pyramidal cells, $u_{Py}(t)$. Those dynamic states are: a stable node, N_1, a low-frequent limit cycle, LF_1, a high-frequent limit cycle, HF_1, and a stable focus, F_1 (see Fig. 3A). The dynamic state depends on the incoming input pulse rate to the pyramidal cells of each area as well as on the initialization (at $t = 0$) of the four state variables (because of multistable regimes).

The time course of $u_{Py}(t)$ of each area constituted the output of each area in the network and was propagated to a set of 62 EEG sensors by means of a propagation matrix, which was already included in the according TVB dataset. The propagation matrix was calculated using OpenMEEG implementing a boundary element method (BEM). The three-shell BEM model was constructed with the MNI Colin 27 dataset,

Table 1
Abbreviations of cerebral areas.

A1	Primary auditory cortex	PFCdm	Dorsomedial prefrontal cortex
A2	Secondary auditory cortex	PFCm	Medial prefrontal cortex
Amyg	Amygdala	PFCorb	Orbitofrontal cortex
CCa	Anterior cingulate cortex	PFCpol	Pole of prefrontal cortex
CCp	Posterior cingulate cortex	PFCvl	Ventrolateral prefrontal cortex
CCr	Retrosplenial cingulate cortex	PHC	Parahippocampal cortex
CCs	Subgenual cingulate cortex	PMCdl	Dorsolateral premotor cortex
FEF	Frontal eye field	PMCm	Medial premotor cortex
G	Gustatory area	PMCvl	Ventrolateral premotor cortex
HC	Hippocampal cortex	S1	Primary somatosensory cortex
IA	Anterior insula	S2	Secondary somatosensory cortex
IP	Posterior insula	TCc	Central temporal cortex
M1	Primary motor area	TCi	Inferior temporal cortex
PCi	Inferior parietal cortex	TCpol	Pole of temporal cortex
PCip	Cortex of the intraparietal sulcus	TCs	Superior temporal cortex
PCm	Medial parietal cortex	TCv	Ventral temporal cortex
PCs	Dorsal parietal cortex	V1	Primary visual cortex
PFCcl	Centrolateral prefrontal cortex	V2	Secondary visual cortex
PFCdl	Dorsolateral prefrontal cortex		

registered with the respective cortical surface from the TVB dataset. Each area instantaneously transmitted the mean firing rate of its pyramidal cell population to other connected areas.

To account for the influence of tDCS we relied on the fact that electric fields affect neurons in a geometry-dependent fashion (Bikson et al., 2004). In this context, the tDCS-induced polarization effect of the resting membrane potential was modeled through a perturbing voltage offset $\overrightarrow{u}_{tDCS}$ to the mean membrane potential of the pyramidal cells subpopulation (see Fig. S2). This approach is known as the "λE model" in comparable modeling studies (Merlet et al., 2013; Mina et al., 2013; Molaee-Ardekani et al., 2013). In the "λE model" the influence of the electric field is represented as perturbation (i.e., an additive voltage ΔV) of the mean membrane potential of a neural mass. The model considers the directionality of the electric field and an altered excitability through the perturbed membrane potential. Although Molaee-Ardekani indicated an effect of tDCS to interneurons, we restricted our analysis to pyramidal cells, because the contribution of interneurons is small (Merlet et al., 2013; Mina et al., 2013; Molaee-Ardekani et al., 2013) and to limit the number of free parameters. A more profound debate on this assumption is included in the Discussion section.

We determined a spatially distributed tDCS influence. For each cortical area (i.e., each node in the network) we computed an individual voltage offset $\overrightarrow{u}_{tDCS}$ as described by.

$$\overrightarrow{u}_{tDCS} = \hat{u}_{tDCS} \cdot \overrightarrow{\zeta}, \qquad (6)$$

The factor $\hat{u}_{tDCS}$ globally scaled the strength of tDCS and was restricted to not exceed an absolute value of 4 mV, corresponding to the polarizing effect of an electric field of 30 mV/mm (Bikson et al., 2004), as employed in a comparable modeling study (Molaee-Ardekani et al., 2013). The factor $\overrightarrow{\zeta}$ represented the spatial distribution of tDCS impact on each cortical area. The basis for this distribution is the current density distribution on the cortical surface – a consequence of the externally applied field. The current density was computed by means of a finite element model (FEM), as described below.

Because tDCS was assumed to maintain a time constant electric flow field over the entire treatment process, $\overrightarrow{u}_{tDCS}$ was held time constant also. This allowed the mathematical transformation of the additive voltage $\overrightarrow{u}_{tDCS}$ into an equivalent tDCS-induced and area-specific additive mean firing rate $\overrightarrow{u}_{tDCS}$ that entered each pyramidal cell population through the path of the excitatory interneurons (see Fig. S2). Thus, Eq. (6) became

$$\overrightarrow{m}_{tDCS} = \hat{p}_{tDCS} \overrightarrow{\zeta} \qquad (7)$$

where $\hat{p}_{tDCS}$ scaled the maximum additional firing rate and was calculated according to the values of $\hat{u}_{tDCS}$ as in.

$$\hat{p}_{tDCS} = \frac{\hat{u}_{tDCS}}{A_{h_e}} \qquad (8)$$

where A_{h_e} was the integral over the time constant kernel of the pulse-to-wave state transformation (see Eq. (3)) and equaled $H_{e,i} \cdot \tau_{e,i}$. Thus, the input to the pyramidal cell population of each area, $\overrightarrow{p}_{in}$, comprised three separate components: (i) a time constant driving input of 108.5 pulses per second, which was used to tune the working point of the local model, (ii) the time constant and area-specific tDCS perturbation $\overrightarrow{m}_{tDCS}$, and iii) the dynamic input which was received from connected areas. Thus, $\overrightarrow{p}_{in}$ reads.

$$\overrightarrow{p}_{in} = \overrightarrow{p}_0 + \overrightarrow{m}_{tDCS} + \gamma \mathbf{W}_{het} S\left(J\left(\overrightarrow{u}_{Py}\right)\right), \qquad (9)$$

where the operator $J(\overrightarrow{u}_{Py})$ described the processing within a Jansen-Rit model.

Current density distribution on the cerebral surface

In order to derive the spatial distribution of tDCS impact on each cortical area, $\overrightarrow{\zeta}$, the current density distribution generated by tDCS was simulated in a finite element model. The finite element model was derived from the same cerebral surface as the large-scale brain network model and surrounding layers comprising the inner and outer skull surface as well as the scalp surface. The volumes of scalp, skull, cerebrospinal fluid (CSF), and brain were meshed to about $2.2 \cdot 10^6$ geometry–adapted hexahedral elements. Stimulating rubber electrodes of (5×7) cm^2 were modeled in a 4 mm dilated scalp mesh (anode: left motor area; cathode: right orbit). The cut-open FEM model visualizing all compartments is shown in Figure S3. Homogeneous conductivity values of 1.4 S/m, 0.43 S/m, 0.025 S/m, 1.79 S/m, and 0.33 S/m (Wagner et al., 2014) were defined for finite elements in electrode, scalp, skull, CSF, and brain compartments. The tDCS simulation of the current density in all elements was performed in the open source software SimBio (Wagner et al., 2014) with an input current strength of 1 mA applying homogeneous Neumann boundary conditions at the scalp surface and inhomogeneous Neumann boundary conditions at the electrode surfaces (Wagner et al., 2014).

Incorporating tDCS in the large-scale brain network model

To determine the area-specific spatial distribution of the tDCS induced perturbation, $\overrightarrow{\zeta}$, current density values of the tDCS forward solution of the brain volume, $\overrightarrow{r}_{FEM}$, were mapped to the 74 areas in the following way:

The three FEM elements, $\overrightarrow{r}_{FEM_{i,k}}$, of the forward model, which lie closest to each of the 16,384 network vertices of the cerebral surface mesh, i, were determined according to the Euclidian norm (i.e., spatial mapping). The magnitude of each contributing current density vector $\overrightarrow{r}_{FEM_{i,k}}$ was multiplied with either +1, for anodal contribution, or −1, for cathodal contribution, according to the dot product between $\overrightarrow{r}_{FEM_{i,k}}$ and the normal vector of the respective surface vertex $\overrightarrow{n_i}$. This ensures that an anodal stimulation perturbs the membrane potential of the respective pyramidal cell population positively, and a cathodal stimulation perturbs the membrane potential of the respective pyramidal cell population negatively. The current densities values of $\overrightarrow{r}_{FEM_{i,k}}$ were averaged to compute the magnitude in the respective surface vertex $\overrightarrow{n_i}$ (i.e., functional mapping). The activity of all vertices i belonging to one area, j, were averaged and scaled to a range between −1 and +1. Thus, the tDCS induced activity in each area, j, was determined by.

$$\overrightarrow{\zeta}_j = \frac{1}{N_j} \sum_{i=1}^{N_j} \frac{1}{N_{CN}} \sum_{k=1}^{N_{CN}} -\text{sign}\left(\overrightarrow{n_i} \cdot \overrightarrow{r}_{FEM_{i,k}}\right) \cdot \left|\overrightarrow{r}_{FEM_{i,k}}\right|^2, \qquad (10)$$

where $N_{CN} = 3$ was the number of the considered FEM elements of the forward model for each surface vertex, and N_j was the number of vertices belonging to one area j. This procedure was visualized in Fig. S4.

Connectivity strength variation

Because a single Jansen-Rit model exhibits various dynamic states depending on the input level, the input to each area was varied by setting the connectivity scale factor for the connectome between $-200 \leq \gamma \leq 350$ with a step size of 0.1. The model equations were solved with an improved Euler method, which was already included in *The Virtual Brain* environment, and a time step size of 0.5 ms.

For $\gamma = 0$, the coupling among the areas vanished and the initial conditions for the lower and the upper stable state of the equilibrium curve were determined analytically. Further initial conditions were found semi-analytically by stepwise continuation of those equilibrium conditions. For sections where this approach was not feasible (i.e., folding of the equilibrium curve), initial conditions were found as the last state vector in a leadoff simulation. To account for settling effects, each simulation of 65 s was run twofold with the last state vector of the first simulation as the initial condition for the second simulation.

For better assessment of the effect of tDCS, we included values of the maximum voltage scaling, $\hat{u}_{tDCS}$, in a range between 0 and 4 mV in 0.5 mV steps in our simulation. We examined the membrane potential u_{Py} of the pyramidal cell subpopulations in an analysis window of the last 16 s of the time series. The baseline potential of each area was extracted and the power spectral density was calculated by means of Welch's method (mean free signal, Hanning window, fast Fourier transform (FFT) length of 8 s, no overlap). Within the frequency range of 0 to 15 Hz, the frequency component with the highest power was extracted as the dominant rhythm of one area. To avoid artifacts from dynamic states like a stable focus, the dominant rhythm was set to zero if the difference between the maximum and the minimum potential within the analysis window was smaller than 1 μV (i.e., the variance criterion). This procedure was depicted in Fig. S5. For the time courses in both the source and the sensor space, the power spectral density was calculated and averaged over eight segments, each of 8 s duration without overlap.

Significant functional connectivity in the source and the sensor space was found by means of Pearson's correlation coefficient and a p-value of less than 0.05. Positive correlation values exceeding 0.8 were extracted for the rest condition and the stimulation condition.

Results

Simulations of the large-scale brain network model were performed under rest (unperturbed) and stimulation (perturbed) as a function of the connectivity scale factor, γ, which globally amplified each weight of the heterogeneous connectivity matrix given by the connectome. Investigating changes during stimulation (with regard to rest), the model showed: (i) an increase in functional connectivity among cerebral areas and scalp electrodes; (ii) more harmonic oscillations (a sharpening of brain areas' frequency spectrum); (iii) an acceleration of brain rhythms at specific sensors, but (iv) an overall deceleration of rhythms across brain areas and sensors; and (iv) a power increase or decrease of the dominant rhythms in the vicinity of the anode or cathode, respectively.

Network state during rest

By characterizing the PSPs of pyramidal cells in terms of baseline and dominant rhythm in rest condition, various network states could be identified in dependence on the connectivity scale factor. According to the transitions across the connectivity scale factor, γ, the network states were divided into nine regimes (see Fig. 2C). A detailed description of the regimes and the transitions are presented in the Supplementary material. The interactions of the areas gave rise to multistable (e.g., 117.6 < γ < 143.9), synchronized (e.g., 33.4 < γ < 117.5) or even chaotic regimes (e.g., 13.6 < γ < 33.3). Investigating the transitions of qualitatively different network states, we found stepwise (e.g., 9 < γ < 13.5) and point-like transitions (e.g., at γ ≈ 33.4) with respect to the connectivity scale factor, γ, for the underlying connectome. Given the transitions existing in an isolated Jansen-Rit model with respect to a constant input level to the PSP of pyramidal cells (see Fig. 3A), the stepwise transitions could be identified as stretched critical ranges in which areas underwent a bifurcation (i.e., an instability) at different connectivity scale factors of the connectome, γ. The point-like network state transition, however, could not be traced back to mechanisms in an isolated Jansen-Rit model.

A comparison of each area's activity in the network with the repertoire of an isolated one revealed the emergence of qualitative new dynamics through network interactions (see Fig. 3C). As a result of network effects, both baseline potentials and dominant rhythms occur out
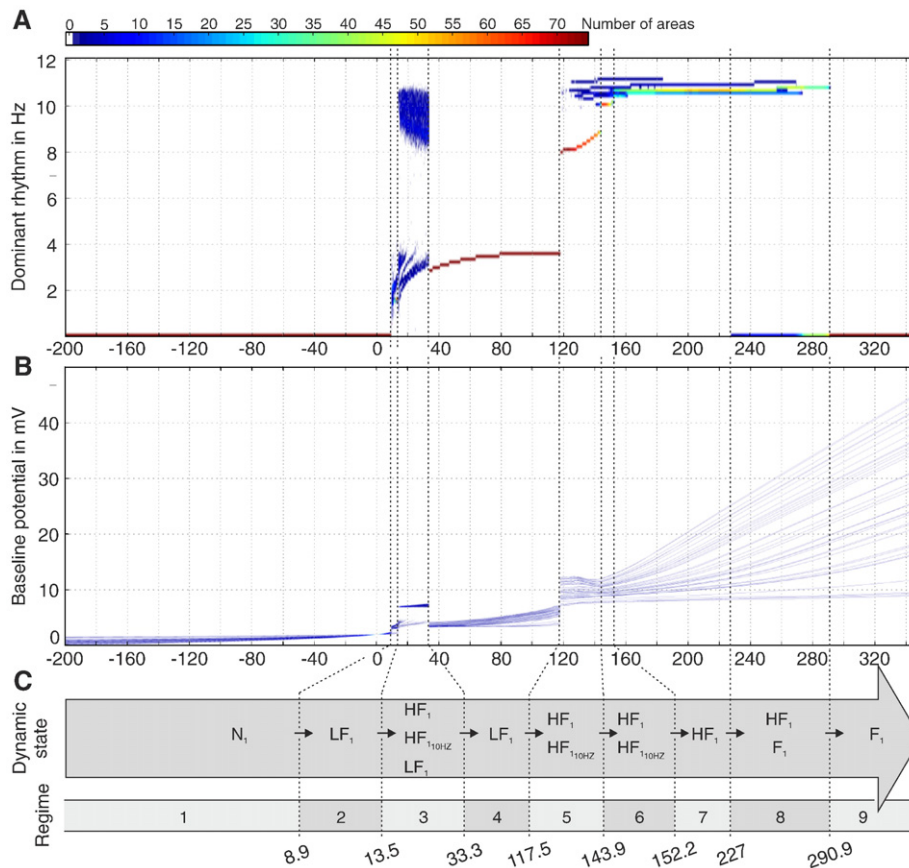

Fig. 2. Network state diagram of the large-scale brain network model during rest. Histogram across areas with regard to connectivity scaling for: **A** the dominant rhythm, and **B** the baseline potential. Panel **C** features the identified network states and regimes.
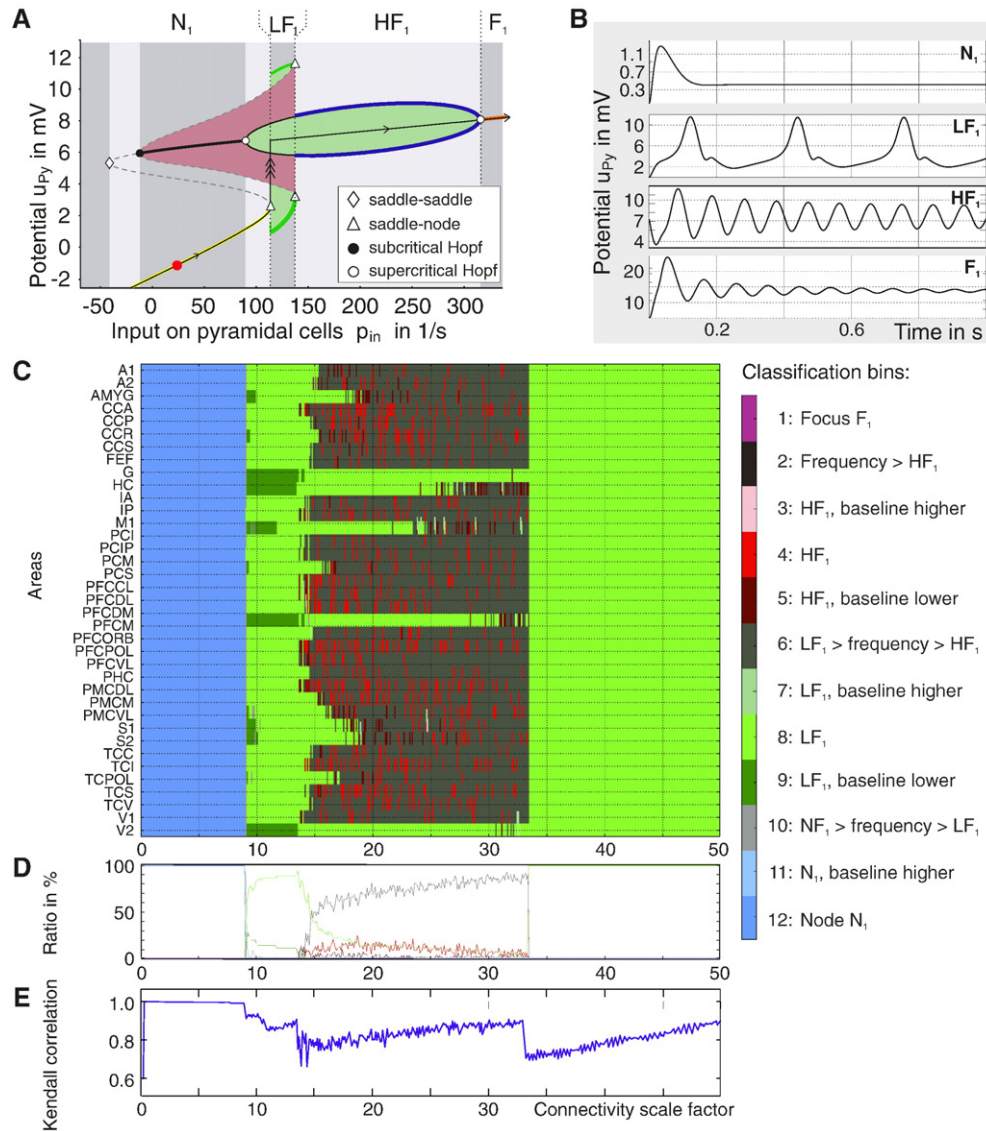
Fig. 3. An area's state changes with increasing network connectivity during rest. The bifurcation diagram of an isolated Jansen-Rit model, as in panel **A,** shows the dynamic repertoire of four dynamic states, i.e. N_1, LF_1, HF_1, and F_1 (Spiegler et al., 2010), distinguishable by baseline potential and occurring frequency. Panel **B**: Initializing an isolated Jansen-Rit model in an unexcited state (see ret. dot in panel A), the model generates constant output in the regime of a stable node, N_1, slow and fast oscillatory output in a limit cycle regime, LF_1 and HF_1, and a damped oscillatory output in the regime of a stable focus, F_1, in dependence on the constant input to the pyramidal cell subpopulation. The dynamic state of each of the interconnected areas in the network circuitry was classified with respect to the repertoire of an isolated area, as in panel **C**. The classification bins are depicted on the right side in panel C. Classification evaluated compliance of each area's dominant rhythm (first criterion) and baseline with those in an isolated area. Note that the classified behaviors 1, 2, 3, and 10 were not exhibited within this range of the connectivity scale factor. New states were found as a result of network interactions. The probability of a state across areas is shown in panel **D**. Correlation of the network structure and baseline potentials are measured by Kendall's tau in panel **E**. The transitions of network states show either an avalanche-like transition or an abrupt state change of areas. With increasing connectivity scaling, the structure increasingly influenced the occurring dynamics up to critical scaling values for which the network reorganized and structure lost ground to the dynamics.

of the usual limits of an isolated area. To assess whether a network state was subject to the area's intrinsic properties, to the network properties, or both, the areas' baseline PSPs (i.e., of the pyramidal cells) were correlated to the in-strengths of the connectome, representing the network structure (see Fig. 3E). For certain ranges of the connectivity scale factor, marked by point-like transitions or the edges of stepwise transitions, this correlation first increased and then abruptly crashed due to reorganization within the network.

Network state during tDCS

Since the structural connectivity indicates the sensitivity of areas for activity-related changes within the network (i.e., the in-strength, see Fig. S1), we compared the strength of tDCS on each area, $\vec{u}_{tDCS}$, with the in- and out-strength of the connectome (see Fig. S6). The tDCS

strength on the cerebral cortex was obtained by a high-resolution finite element forward calculation (see section *Materials and methods*). The right anterior cingulate cortex (rCCa) and left medial prefrontal cortex (lPFCm) were most affected by tDCS (the former anodal and the latter cathodal), and the primary motor cortex (M1) was least affected by tDCS. Since rCCa and lPFCm featured a higher in- and out-strength than average (across areas), while in- and out-strength were moderate for M1, we expected rCCa and lPFCm to be more affected by tDCS than M1.

Analogous to the resting state condition, we characterized the dynamic network state during tDCS dependent on the connectivity scale, γ, and the scale factor for the tDCS strength, $\hat{u}_{tDCS}$. The network states during tDCS were compared to those found during rest in Fig. 4. During tDCS, the areas expressed their individual intrinsic behavior for wider ranges of the connectivity scaling, γ, as apparent from the spread of

dominant rhythms and baseline PSPs over connectivity scales across areas with increasing tDCS strength. The main differences between the network state during rest and stimulation occurred for connectivity scaling up to $\gamma \leq 120$. For higher scaling, $\gamma > 120$, the network states were qualitatively equal during rest or stimulation. Across all tDCS scaling factors, tDCS gave rise to negative baseline potentials, which were previously positive during rest. Primarily, this shift in baseline potentials was caused by the selective cathodal (i.e., negative) offset and was more prominent for small as well as negative values of γ. The higher the scale for the tDCS strength, the lower the connectivity scale factor, γ, for which areas exhibited the first oscillations. The connectivity scaling, γ, at which areas started oscillating slowly (<4 Hz) was $\gamma = 8.9$ during rest and $\gamma \approx -30, -100, -185,$ and < -200 during tDCS for a tDCS scaling, $\hat{u}_{tDCS} = 0.5, 1, 1.5,$ and 2 mV, respectively. With increasing strength of tDCS, fast rhythms (>8 Hz) set in with smaller connectivity scaling, γ. The connectivity scale, γ, at which areas started showing fast rhythms (>8 Hz), was $\gamma = 13.6$ during rest and $\gamma \approx 10, -40, -185,$ and < -200 during tDCS with a scaling, $\hat{u}_{tDCS} = 0.5, 1, 1.5,$ and 2 mV, respectively. Interestingly, at $\hat{u}_{tDCS} = 1.5$ mV, fast and slow rhythms started simultaneously from $\gamma \approx -185$ on, interrupted by a silent regime between $-130 < \gamma < -95$ (almost no oscillations). Furthermore, the expansion of fast rhythms to negative connectivity scaling for increasing

strength of tDCS came along with a smaller variance across areas. In contrast, the variance of fast rhythms for connectivity scaling factors, $\gamma > 10$, during rest and stimulation was remarkable. Another qualitative change occurred in the connectivity scaling range of $33.4 < \gamma < 117.5$. During rest, this range spanned a regime of synchronized low rhythms (3–4 Hz) bounded by two abrupt transitions at $\gamma = 33.4$ and $\gamma = 117.5$ (see Fig. 4). During stimulation, these two transitions converged ($\hat{u}_{tDCS} = 0.5$ mV: $82 < \gamma < 115$ and $\hat{u}_{tDCS} = 1.0$ mV: $83 < \gamma < 95$) and vanished ($\hat{u}_{tDCS} > 1.0$ mV) with increasing strength of tDCS. Slow rhythms vanished for $\hat{u}_{tDCS} > 1.0$ mV and, instead, two separate fast rhythms (~11 Hz and 8–9 Hz) became stable, diverging with increasing connectivity scaling. Interestingly, for $\hat{u}_{tDCS} = 1.0$ mV a stable slow rhythm existed ($83 < \gamma < 95$), but the two abrupt transitions were smoothed out for the two fast rhythms forming a tristable regime (~3.8 Hz, ~8.2 Hz, and ~10.5 Hz). For $\hat{u}_{tDCS} = 0.5$ mV, similar tristable regimes existed for a connectivity scaling range of $48 < \gamma < 82$ and at $\gamma = 114$.

Functional connectivity and synchronization during tDCS

Because the network state for a connectivity scaling range of $13.6 < \gamma < 33.3$ was found with high variance in fast rhythms during
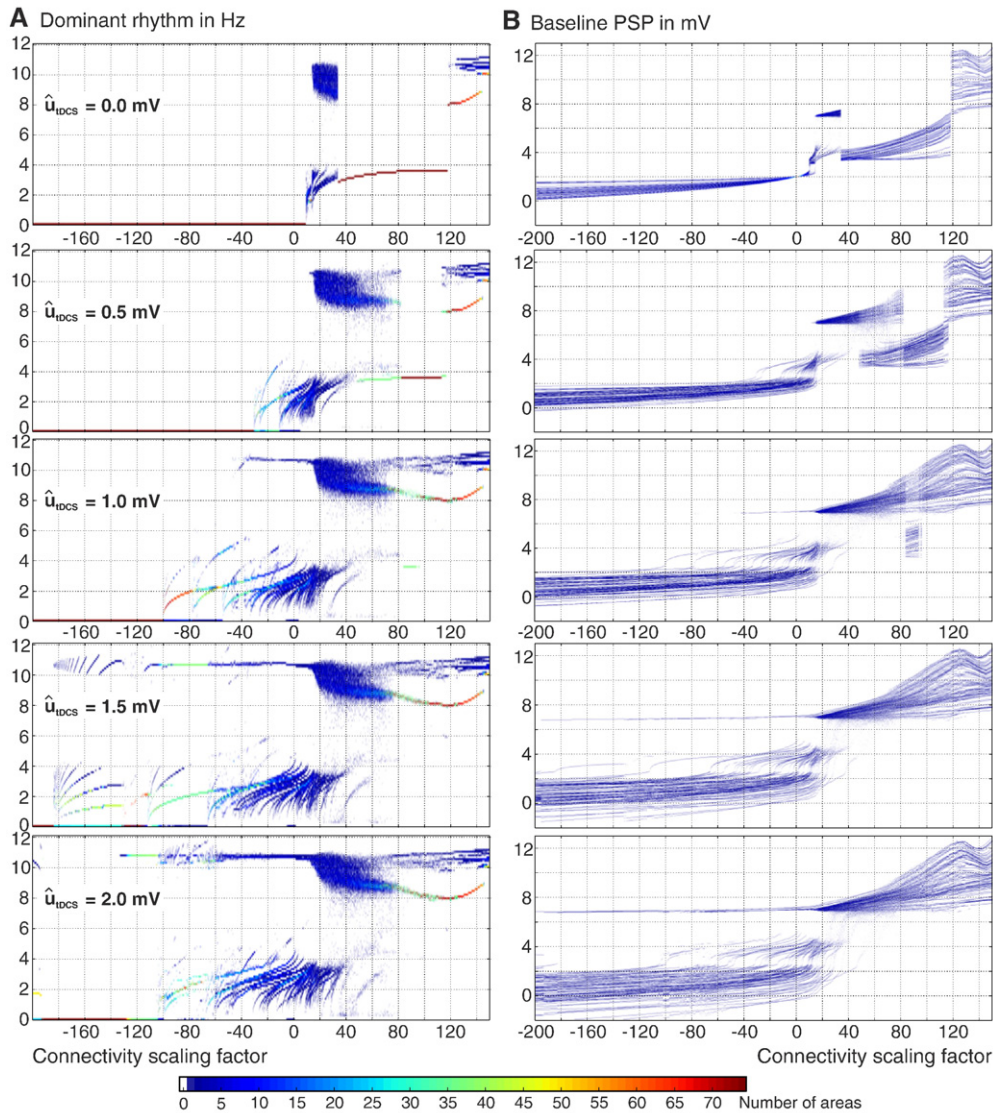

Fig. 4. Effect of scaled tDCS on the cerebral area. The histograms of the dominant rhythms, in panel **A**, and baseline potentials, in panel **B**, are depicted during rest (top row) and during stimulation with increasing scaling (second to fifth row).

tDCS and in rest (see previous paragraph), we examined this chaotic regime in more detail to find out whether tDCS affects the interplay in the network or simply modulates the dynamics.

Regarding the 62-channel EEG for an exemplary connectivity scale factor of $\gamma = 22$, oscillations in the alpha-band were dominant in 53 channels during rest and 42 channels during tDCS ($\hat{u}_{tDCS} = 4$ mV), where other channels showed oscillations in the delta-band (<4 Hz) (see Fig. 5). This reflected an observation from the cerebral areas, namely that tDCS slows down the dynamics. Another observation was that tDCS made the oscillations more harmonic (indicated by a sharpening of the frequency spectrum with clearer peaks). EEG channels covering the region of the anode (i.e., C3, C5, CP1, CP3, and CP5) and cathode (i.e., Fp2, AF4, AF8, F4, and F6) kept their main power in the alpha-band during tDCS, but with considerably reduced power in the latter and increased power in the former case (see Fig. 5). For all electrodes in both groups, the power peak was slightly shifted to higher frequencies (~11 Hz). The right parietal channels (P2, P4, P6, PO4, and PO8) behaved similarly to the channels covering the anodal region. Interestingly, tDCS quashed oscillations in frontocentral channels (F1, Fz, and F2), indicated by a dramatic power reduction in the frequency spectrum (see Fig. 5). Contralateral to the anode, central and centroparietal channels (C4, C6, T8, CP2, CP4, CP6, and TP8) maintained the power in the alpha-band, but exceeded by a power increase in the delta-band during tDCS. For occipital channels (O1, Oz, and O2), the oscillations in the delta-band lost power, but remained dominant during tDCS.

To assess the functional connectivity among cerebral areas (Fig. 6A) and in the scalp EEG (Fig. 6B), we chose two exemplary connectivity scale factors, $\gamma = 22$ and $\gamma = 30$. For both scaling factors, the areas establishing strong correlations (> 0.8) during tDCS (red marks in Fig. 6A) were located more in the left (i.e., left upper quadrant) than in the right hemisphere (i.e., right lower quadrant). Almost none of the strongly correlated areas during rest maintained their correlation level (blue marks) but vanished under stimulation (green marks in Fig. 6A). Please

note the similarity of the functional connectivity pattern between the two connectivity scale factors in Fig. 6A. On the scalp, the electrodes establishing correlations during tDCS (red lines) were clustered in three regions for $\gamma = 22$ (Fig. 6B). Two regions reflected the sites of the anode (i.e., C3, C5, T7, CP3, and CP1) and the cathode (i.e., Fp2, AF4, AF8, F4, F6, and F8), including neighboring areas (i.e., FC2, FC4, and FC6) in the latter case. A third region covered the right central line, that is, T8, C6, C4, CP2, and CPz. Since our model mainly features oscillations in the alpha band, the increased functional connectivity at the cathode qualitatively reproduced former experimental results of resting state activity before and after a tDCS treatment, see Fig. 3 in (Polania et al., 2011a). For the higher connectivity scaling, $\gamma = 30$, the anodal correlation cluster appeared as well, whereas the cathodal cluster was much less pronounced and the central cluster no longer existed (Fig. 6B). Although an agreement with the empirical results is unsatisfying for the higher connectivity scaling factor, $\gamma = 30$, the underlying functional connectivity maps on the level of cerebral areas were similar. For both scaling factors, $\gamma = 22$ and $\gamma = 30$, a correlated parietal region on either side maintained correlated during tDCS (blue lines), although some connections vanished (green lines).

The emergent functional connectivity among areas and EEG electrodes suggested synchronization to be the underlying mechanism. Indeed, all 74 cerebral areas oscillated within the connectivity scaling range of $13.6 < \gamma < 33.3$, during both rest and tDCS. For $\gamma = 22$, 64 areas oscillated fast during rest and 52 areas during tDCS ($\hat{u}_{tDCS} = 4$ mV), which indicated that tDCS slows down brain rhythms. However, the cerebral areas contributed the most to the emerging correlated anodal cluster on the scalp during tDCS essentially maintained their dynamic behavior (see Fig. S7). The frequency spectrum of these areas became sharpened (i.e., clearer peaks and thus more harmonic oscillations) with an increased and a slightly shifted power peak, indicating synchronization during tDCS (see Table 2 for a comparison of the variance). In contrast, two of the four cerebral areas contributed the most to the emerging correlated cathodal cluster on the scalp during tDCS
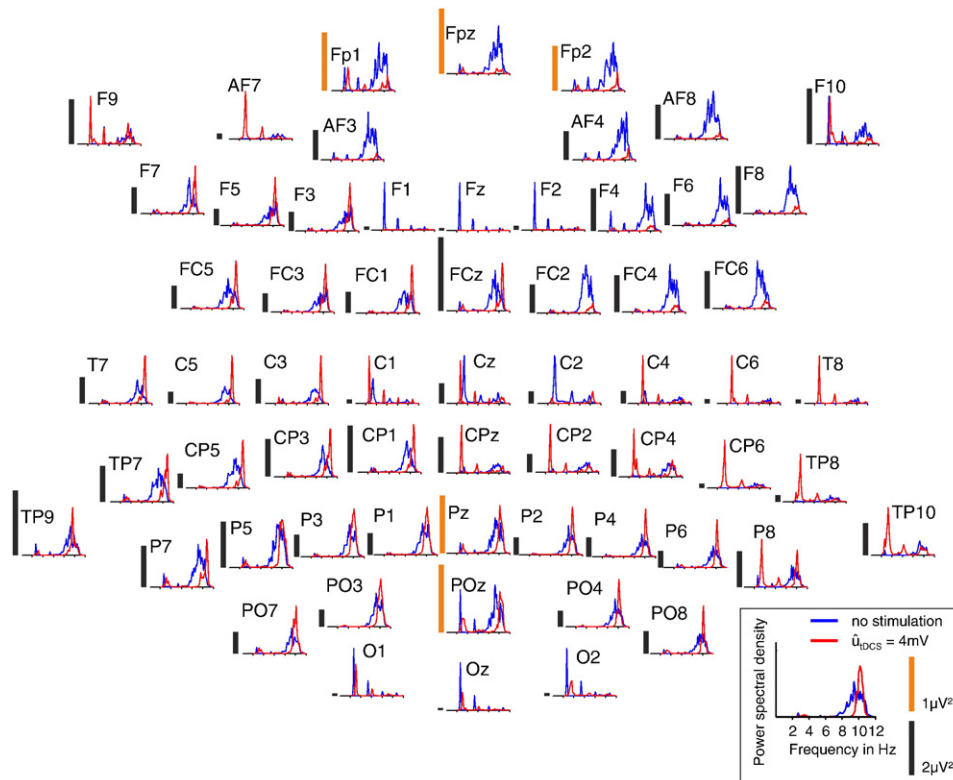

Fig. 5. Spectral changes in EEG during tDCS ($\gamma = 22$, $\hat{u}_{tDCS} = 4$ mV) with regard to rest. Under rest and during stimulation, rhythms occurred mainly in the alpha and the delta-band. Rhythms occurred more harmonic during tDCS (sharpening of frequency spectra with clearer peaks) and either decelerated or accelerated.
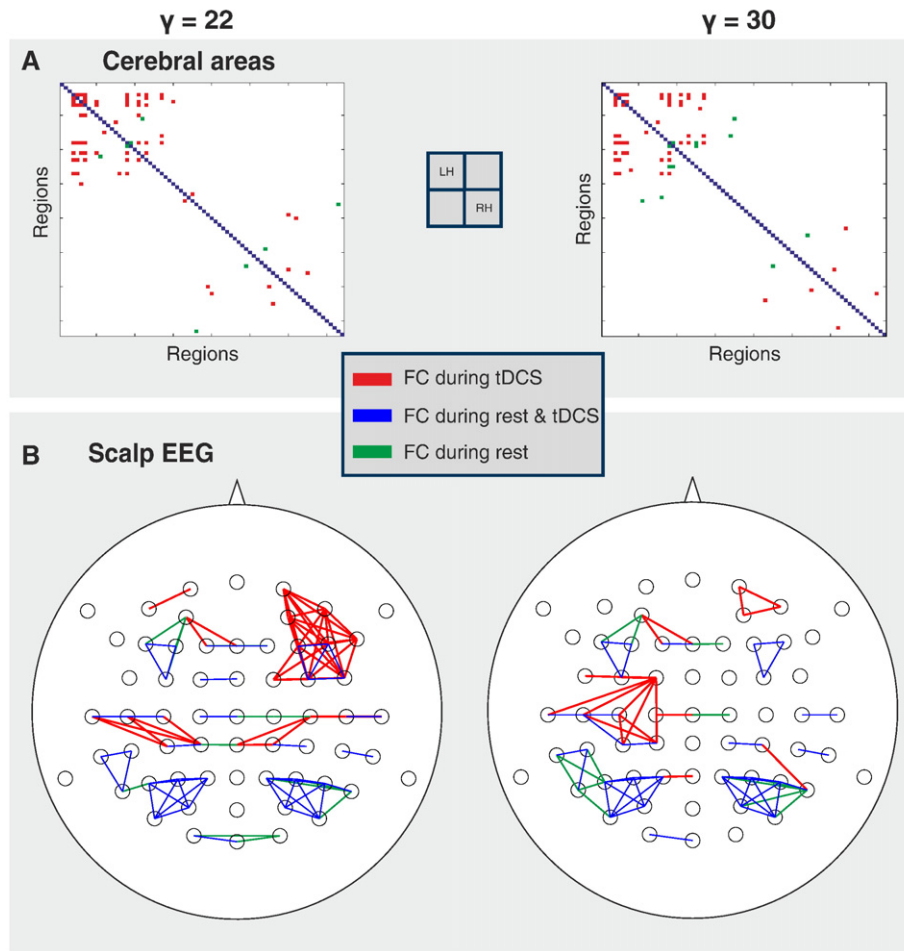
Fig. 6. Functional connectivity changes during tDCS of cerebral areas and in EEG. Panel **A**: Functional connectivity of areas for $\hat{u}_{tDCS} = 4$ mV and $\gamma = 22/30$. White marks label correlations that did not exceed a threshold of 0.8. Blue marks label correlations that exceeded the threshold and were present during rest and tDCS. Green marks label correlations that occurred only during rest and red marks label correlations that arose during tDCS. Panel **B**: Functional connectivity in scalp EEG sensors with the identical color-coding.

(i.e., left and right PFCdm) switched to a fast rhythm (see Fig. S8). The other two areas (i.e., right PFCdl and PFCcl) continued to oscillate fast, but with significantly less power and highly modulated with lower frequencies. The baseline PSPs of the areas in the vicinity of the anode were mostly elevated whereas the baseline PSPs of areas in the vicinity of the cathode were mostly reduced. See Table 3 for a comparison of baseline PSPs and variance under rest and stimulation.

Discussion

The positive clinical effects of transcranial direct current stimulation (tDCS) are presumably caused by the complex interactions between the brain network and the electrical current of the stimulation. In this study, we examined the network mechanisms through which tDCS becomes effective. Our modeling approach allows for the investigation of spatio-temporal brain activity on the level of sources and sensors with regard to the interplay of structure and functional behavior. We observed and

cataloged various connectivity-dependent network states for further use in other modeling scenarios. In particular, we found an increased connectivity among cerebral areas and among EEG sensors, where the latter reproduces the measurements by Polania and colleagues (Polania et al., 2011a). A further analysis of the network dynamics identified synchronization as the main mechanism of the observed effects. Furthermore, the frequency distribution of scalp EEG sensors was sharpened and slightly shifted towards higher frequencies during tDCS. Due to the complex interaction within the network, novel dynamic states emerged, extending the known dynamic states of an isolated Jansen-Rit model.

Functional connectivity during tDCS

It was possible to show that tDCS robustly induces additional functional connections both on the sensor and the source level. The tDCS-caused changes in the functional connectivity potentially bias (e.g., activate or deactivate) certain functional networks. Evidence that

Table 2
Baseline in mV (Variance in mV^2) of the areas under the anode during tDCS for $\gamma = 22$.

Area	Rest	$\hat{u}_{tDCS} = 4$ mV
Left S1	7.012 (1.724)	7.406 (1.361)
Left PCs	7.184 (2.862)	7.242 (1.740)
Left FEF	7.027 (3.968)	7.437 (1.759)
Left PCi	7.143 (3.917)	7.672 (1.253)
Left PCm	7.081 (1.307)	1.405 (<0.01)

Table 3
Baseline in mV (Variance in mV^2) of the areas under the cathode during tDCS for $\gamma = 22$.

Area	Rest	$\hat{u}_{tDCS} = 4$ mV
Right PFCdm	3.829 (2.207)	7.151 (0.969)
Right PFCdl	7.154 (6.424)	1.589 (<0.01)
Left PFCdm	3.776 (2.782)	0.224 (<0.01)
Right PFCcl	7.012 (1.724)	−0.231 (<0.01)

tDCS alters the functional organization of cortical processing was provided in former studies (Polania et al., 2011a; Sehm et al., 2012). A targeted bias of functional networks might explain the numerous positive effects that tDCS has on neurological and psychiatric diseases (Antal et al., 2010; Fregni and Pascual-Leone, 2007; Lindenberg et al., 2010; Nitsche et al., 2009). Furthermore, stimulation effects might depend on the current behavioral state of the brain itself (Northoff, 2012; Northoff et al., 2010; Silvanto et al., 2008). In this study, the brain state (i.e., the internal condition of the brain) was assumed to be a resting state, that is, the state of the brain in the absence of any given task and overt stimuli, for instance, awake with eyes closed (Logothetis et al., 2009; Raichle, 2010). Furthermore, there is evidence that an increased functional interaction or connectivity leads to structural changes in gray matter through synaptic plasticity (i.e., long-term potentiation) and in white matter through changes in axon caliber and myelination (Gibson et al., 2014).

Effect of tDCS on the cortex

In extension to forward modeling tDCS studies (Bikson et al., 2012; Ruffini et al., 2014), our approach emphasizes the importance of the spatiotemporal organization of the brain in terms of structure and function as dynamics. Instead of relying on precise spatial current distributions to assess tDCS effects, our approach underscores tDCS as a neuromodulatory technique causing the brain not only to react but also to adopt its behavior during stimulation. Nevertheless, our FEM volume conductor model for tDCS forward simulations comprises the sensitivity-wise critical compartments: skull, CSF and the folded brain (Opitz et al., 2015; Wagner et al., 2014). Rather than limiting tDCS effects to a spatially constrained model (Molaee-Ardekani et al., 2013), we use a large-scale brain network model to allow for signal propagation following tDCS (Bikson et al., 2012; Fox et al., 2014; Ruffini et al., 2014). During tDCS the mean PSP of pyramidal cells in each area was constantly shifted towards higher or lower values according to the spatial current density distribution. Because the topology of an area in the network is unique for each area (i.e., connectivity fingerprint), two considered areas will be differently modulated by their respective connected areas and thus respond differently to the same tDCS input on the large-scale level of global interaction. The current density distribution was obtained with the help of a high-resolution finite element model of two tDCS electrodes on the scalp. The observable negative baseline PSPs during stimulation (see Fig. 4) were primarily specific for the utilized oscillator model (see Fig. 3A). Furthermore, cathodal influence to the areas reduced the PSPs for small values of $|\gamma|$. For large values of γ ($\gamma > 120$), the influence of connected brain areas dominated the tDCS offset in each of the single areas. Positive high values of γ amplified input from connected areas while high negative values of γ led to a complex interplay between negative amplification and damping due to the saturation of the transfer function. This effect of tDCS on the cortex generally leads to a spatially specific adjustment of cerebral areas (see Tabs. 2 and 3).

In the absence of cortico-cortical connections, the dynamic state of each area would be set by tDCS. However, taking cortico-cortical connections into account, tDCS did not only affect a single area directly, but also the interactions between areas of the brain (see Fig. 3). Merlet and colleagues studied the tACS effect on the cortex by separated cerebral areas, but all connected via one thalamic area (Merlet et al., 2013). This study could not provide insights in the spatial reorganization of brain dynamics due to tACS. This is why we focused on the interplay of tDCS and the structural connectivity of cerebral areas. Our findings indicate facilitation of alpha activity in fronto-central to parieto-central areas ipsilateral to the anodal electrode over M1. This synchronization leads to an increased local functional connectivity in areas beneath the anodal stimulation electrode. Local functional synchronization due to tDCS has been reported in several studies using EEG (Polania et al.,

2011a), fMRI (Polania et al., 2012; Sehm et al., 2012) and evaluation of paired associative stimulation (Nitsche et al., 2007).

To the best knowledge of the authors, the sharpened and shifted frequency spectra (see figures S7 and S8) represent an effect that was not described in empirical studies yet and ought thus be seen as a prediction of the present model. The measured changes in functional connectivity by Polania and colleagues (Polania et al., 2011a), which were partially reproduced here, propose a modulation of the intrinsic functional network dynamics as a consequence of the polarization. Thus, our study promotes the inclination to develop the identification and understanding of competing network dynamics rather than confine investigation to a highly precise focal stimulation of one particular brain region (Fox et al., 2014; Wokke et al., 2014).

Structure, function, and dynamics

We demonstrated that tDCS does not only locally polarize the membrane potentials of cerebral areas, but also affects the interaction among brain areas. Each area with its intrinsic repertoire of dynamics (e.g., of natural rhythms) was subjected to its embedding in the brain architecture given by the human connectome (input from other areas) as was the interaction between areas, measured as functional connectivity. This way, the topology of the network not only allowed for functional interactions between brain areas, but also established a dynamical regime in each area that was either intrinsic (included in the area's repertoire) or emergent from the interplay in the network. We quantified the network topology by graph theoretical measures (Fornito et al., 2013; Polania et al., 2011b), see Fig. S6, and found that the areas change intrinsic regimes with increasing connectivity strength according to the order of the total strength of incoming ties to an area (i.e., in-strength; see Fig. 3E). Structurally, more dissociated areas from the network reacted less sensitively to changes than associated ones, and thus established inherent regimes. However, the structural topology lost ground to the dynamics when a first brain area changed regimes with increased connectivity scaling (see Fig. 3E). This in turn affected the others, which adjusted dynamics through the interplay in the network and changed regimes in an avalanche-like fashion (see Fig. S9). Because the connectome we used here showed symmetries between the hemispheres (see Fig. S1A), functional areas in both hemispheres behaved similarly.

We found nine different dynamic states in the network by systematically scaling the connectome. If we consider our network of $m = 74$ areas, each with a dynamic repertoire of $n = 4$ qualitatively different states, the network can feature $n^m = 4^{74}$ states at the maximum. Hence, we found a far smaller number of network states than the theoretical maximum. The reason is that the network in our thought experiment, $n^m = 4^{74}$, (i) simply picks an area's state out of the repertoire by the weights of the ties, (ii) omits emergent states out of interactions (e.g., synchronization), and (iii) does not take the specific network topology into account. Considering the structural connectivity by the number of orthogonal patterns, $n = 58$, explaining 95 % of the topology still gives an enormous number of possible network states given the nine states we observed. Once again, our conclusion is that the topology not only constrained the resources throughout the evolution of the dynamics to a small number of states, but also facilitated emergent states through interactions.

Resting-state dynamics

The observed resting-state network dynamics could be understood in large parts in the context of the temporal dynamics of an isolated Jansen-Rit model. Scaling of the connectivity weights among the network areas increased the activation of the areas in terms of baseline PSPs and modulated the intrinsic functional organization (i.e., connection between interneurons and pyramidal cells within an area). With increasing connectivity scaling, areas subsequently exhibited constant activity (Regime

1), slow (Regime 2 and 3), and fast oscillations (Regime 3). A detailed description of the regimes and the transitions are presented in the *Supplementary material*. An insufficient interaction between areas led to a chaotic behavior of weak synchronization and wider distributed, but fast rhythms in Regime 3. Followed by reorganization in Regime 4, a fully synchronized slow rhythm emerged, which is qualitatively new comparing the baseline to the one of an isolated area. Note that almost all dynamic network states can be ascribed to the individual bifurcations in an area, whose undergoing depends on the history and thus causes that hysteresis effect of network states.

These observations underline the notion that even small and short-term variations in connectivity are able to evoke switching of network dynamics (Hansen et al., 2015). This structure–function relationship was also expressed in the correlation of PSPs and the in-strength ranking of areas. Correlation increased with higher connectivity scaling up to a critical value at which the network could no longer balance the functional resources through the structure, and therefore reorganized.

Implication to large-scale brain network modeling

The local model (Jansen and Rit, 1995) we used to describe each area is widely used not only in population studies (David and Friston, 2003; Spiegler et al., 2011; Wendling et al., 2002), but also for large-scale network modeling (Merlet et al., 2013; Sotero et al., 2007) as well as for model inversion in *Dynamic Causal Modeling* (*Pinotsis* et al., *2012*). However, a systematic study of the effects of structural connectivity on the dynamics was missing. Here, for the first time, we cataloged the network states depending on the connectivity scaling. This catalog is specific for the connectome. However, the used connectome is the default one in the open-source neuroinformatics platform, *The Virtual Brain* (TVB) that we used for this study [www.thevirtualbrain.org]. The script we used to perform this study will be part of a demo package for using TVB. Therefore, the results are easy to reproduce and ready to be used for parameterizing models in other modeling scenarios.

In general, the catalog nicely indicates the sensitivity of areas with respect to perturbations. Several phenomena might indicate universal effects of networks regardless of whether connectome or dynamical description is used for the area. First, the network topology and the connectivity weights disperse the areas' state from being homogeneous (see Fig. S9). Secondly, this dispersion causes interactions among the areas in the network, which rebalance and thus reorganize the dynamics. By scaling all network weights equally, such reorganizing behavior undergoes critical phases and divides network states into qualitatively different regimes (see Fig. 2). Thirdly, the transitions from one network regime to another can be abrupt or in an avalanche-like fashion with respect to the connectivity scaling. The avalanche effect can be ascribed to the dispersion effect of the network: A state transition of a single area imposes transitions in other areas throughout the rebalancing processes so that the network state changes stepwise with respect to the connectivity scaling. This effect is likely to occur if several areas are close to an inherent bifurcation. In contrast, the network state changes abruptly if a critical number of areas have passed an inherent bifurcation and a stable network state of the multistable areas cannot be found throughout the rebalancing processes. Consequently, the areas unify to a stable network state of less diverse areas (see Fig. 2). Note that the avalanche-like transition ties to the dynamic repertoire and bifurcations of a single isolated area, whereas the abrupt transition is mainly an effect of the network.

Multistable regimes (see, for example, $13.6 < \gamma < 33.3$ in Fig. 2) show a variety of dynamics that cannot be understood on the basis of a single area model. Such network regimes allow for more plausible modeling of frequency distributions as observable in measurements. Note that in contrast to the deterministic character of our model, other modeling studies introduced noise to obtain realistic frequency distributions (David and Friston, 2003; Wendling et al., 2002). Consequently, our findings for our large-scale brain network model based on Jansen-Rit populations motivate to test different connectomes and local models

under different parameterizations in a similar way to our approach to account for dynamics that resemble brain activity in space and time under different conditions.

The work presented here enables the systematic and elaborated investigation of network dynamics and synchronization phenomena under various conditions, such as the impact of an externally applied electrical current. Furthermore, our approach allows the assessment of the impact of particular connectomes, such as connectomes with special functional or structural features, to the network dynamics. In this manner, there is the potential to better understand functional particularities (e.g., focal or distributed epileptic sources) and structural deficits (e.g., following stroke or a traumatic brain injury). In conjunction with graph theoretical measures, network properties could be related to changes in network dynamics or changes in the environmental conditions, such as through stimulation (Luft et al., 2014; Polania et al., 2011b).

Limitations and simplifying assumptions in the model

The brain network model utilized in this study approximates both structural (e.g., neural circuitry) and functional (e.g., state description solely by means of two state variables per neural mass) qualities of the human brain. Complex and partially well investigated mechanisms were simplified on various levels: i) on the cellular level, e.g. reduction of manifold types of neurons to excitatory and inhibitory neurons (Contreras, 2004) and neglect of single action potentials, ii) on the level of interaction between subpopulations, e.g. via mean values of activity and neglecting any higher order statistics, complex interconnectivity within the laminae of the cerebral cortex, see (Thomson and Bannister, 2003), and iii) on the level of macroscopic interaction, e.g. cortex parcellation and long-range connectivity.

Furthermore, signal transmission via the long-range white-matter fiber tracts is assumed to be instantaneous, neglecting any time delays. Admittedly, such time delays are relevant for the biological plausibility of the model and are likely to modify the dynamics (Deco et al., 2011; Kutchko and Frohlich, 2013), for example collateral oscillations, synchronization motifs, or interference (Pajevic et al., 2014). However, it is not exactly clear under which circumstances delays play a role. According to the Kuramoto model, which approximates the phase interaction of oscillators, effects of delays less than a quarter of a period of the natural frequency of an oscillator are negligible. Because of the rich repertoire of dynamics from a biologically plausible model at each area, it is absolutely not trivial to study the network behavior. In fact, this is the first time that the emergent network effects are systematically analyzed with single-node dynamics defined by Jansen-Rit elements. According to Knock et al. (Knock et al., 2009), a slow transmission speed of $v = 1.5$ m/s is necessary to affect the alpha rhythm, which would be still too fast to affect the slow wave–spike cycle ($0 < f < 4.7$ Hz). Furthermore, high transmission speeds do not affect the network dynamics (Knock et al., 2009). In fact, a transmission speed of 1.5 m/s is quite slow with respect to an average transmission speed for white matter fiber bundles of approximately 6–7 m/s (Nunez, 1995). The considered node dynamics (i.e., Jansen-Rit) are simply too slow to be affected by time delays resulting from biophysically plausible transmission speeds for myelinated axons.

In this work, we work with a connectome-based large-scale brain network model, which seeks to investigate network behavior at the meso- and macroscopical scale of neural populations. The utilized local model, a neural mass model, describes dynamics in an abstract neural population, which is described by averaged state variables as a result of the mean field approach. This type of modeling approach does not aim for explaining microscopic effects of neurons (Reato et al., 2010, 2013) but rather approximates the effects on a mesoscopic level. These models are informative at the large-scale of a whole brain from the point of view: the structure of the brain network (topology) constrains its function and thus the functioning of the brain. Information

about long-range connections is provided by diffusion spectrum imaging data and histological data of primates. Note that both modalities possess major difficulties in terms of their applicability. While diffusion spectrum imaging allows for noninvasive investigation of human structural connectivity, its resolution and specificity (indirect measure) is limited. Also, data lack information on directionality of the connection. However, invasive histological methods are not applicable in living humans. Furthermore, both modalities provide limited information about absolute weight of the connection. Note that due to the symmetry of the connectivity matrix, the utilized connectome does not contain any information on directionality of the connections. The connectome used here did account only for cerebral areas and did not include thalamic areas that can have an important effect on the dynamics (Merlet et al., 2013; Sotero et al., 2007). In the present model we exclusively used forward connections for which the membrane potential of one pyramidal cell population is used as input of the pyramidal cell population of a connected area. The resulting dynamics for the default parameterization are well investigated (Spiegler et al., 2010). We omitted backward and lateral connections with their more complex local connectivity schemes (Felleman and Van Essen, 1991). Current state-of-the-art techniques to map the human brain's large-scale connectivity (i.e., white matter fiber bundles) such as diffusion MRI are blind for connections within the cortex (because the connections in the gray matter are too diffuse), and thus blind for the aborization of axons entering or leaving the cortex forming the white matter fiber bundles (Bota et al., 2015). The directionality of connections in our large-scale brain network model stems from the CoCoMac database (Kotter, 2004), thus based on tracer studies in macaque.

Moreover, the connectome crucially determined the observed spatiotemporal dynamics. Consequently, the quality of the connectome in terms of content and accuracy is of general importance (Van Essen et al., 2013). Each of the 74 cortical areas (i.e., each network node) of the chosen cortex parcellation were modeled by a single NMM and featured the same default parameterization (Jansen and Rit, 1995). However, a single NMM is a spatially abstract and dimensionless system. The complex processes within a biological neural area are abstracted by the interaction of the three considered subpopulations in each NMM. The spatial information is incorporated by the connectivity between the areas. Thus, for the dynamics the shape and size of the region is of lower importance. We chose the same parameterization, adopted from (Jansen and Rit, 1995), for each NMM because: (i) we assume the existence of generic neural mesocircuits, where the function of a region emerges from the interaction in the network, (ii) interregional differences lack in appropriate a priori information, and (iii) we strived to restrict the level of complexity in the brain network model.

We would like to clarify that our model seeks to investigate network behavior at the meso- and macroscopical scale of neural populations. The utilized local model, a neural mass model, describes dynamics in an abstract neural population, which is described by averaged state variables as a result of the mean field approach. By that we follow an established level of abstraction, see (Deco et al., 2008; Spiegler et al., 2010). Admittedly, this type of modeling it not suited to explain microscopic details of neurons and we acknowledge the necessity to achieve a better understanding of microscopic properties underlying the interaction of neurons and electric current, see (Reato et al., 2010, 2013). Although we think that theoretical and experimental findings of microscopic DC-studies are valuable concerning the regulatory mechanisms of the dynamics of the cell membrane, we argue that population models are adequate to better understand the effects on the larger scale of whole brain dynamics.

Note that the brain network model in this work was not driven and all the results are out of deterministic dynamics. Because we found a chaotic network regime that we then also used for analyzing functional connectivity during tDCS, the model provides non-stationary brain signals.

Regarding the forward calculation for the tDCS strength on the cerebral surfaces, the current density distribution was spatially undersampled due to the limited number of cerebral areas given by the connectome. To overcome this issue one could refine the cerebral description by a neural field considering the connectivity on the cerebral surfaces in the vicinity of neurons or neural populations (Sanz-Leon et al., 2015).

The directionality of the electric field relative to the spatial alignment of the neurons is one very important factor for the effect tDCS one the brain network model. It determines whether a local neural population, that is, a network node gets excited or inhibited by stimulation and to which degree. We chose a neural mass approach since the structural connectivity data is based on a coarse grained Brodman parcellation. Each brain area in the network was described by means of mean postsynaptic potentials (PSPs) emerging from the interaction of pyramidal cells with excitatory and inhibitory interneurons, which is the Jansen-Rit model. In this study, we limited the effect of tDCS to the pyramidal cells. Our rationale for this is the following, namely that neuronal currents underlying M/EEG generation are believed to be produced mainly by the membrane potentials of the PCs (Lopes da Silva and van Rotterdam, 1999) as a result of the asymmetric shape of these cells (with apical dendrites) and their parallel alignment perpendicular to the cortical surface (Braitenberg and Schuez, 1991). Consequently, on the level of description we are dealing with, an external electrical field may primarily affect structures that are spatially aligned such as the pyramidal cells in layer IV of the cortex and less the diffuse structures such as interneurons. Another argument is that most neocortical neurons (70–80 %) are excitatory pyramidal neurons and the remaining 20–30 % are interneurons (Markram et al., 2004). These arguments are no reason to exclude the case that tDCS does not also effects interneurons as indicated by (Molaee-Ardekani et al., 2013). However, the rationale for considering tDCS to simply affect pyramidal cells was to limit free parameters and the conclusion by Molaee-Ardekani "that pyramidal cells constitute the neuronal sub-population that is affected the most by tDCS".

The directionality of the current density relative to the normal vector of the cortex surface represents the type of tDCS impact (i.e. anodal or cathodal). The resultant effect strength of the current density was accounted for in the FEM solution. We used the current density estimate because the shapes of the cortical surface create inhomogeneities that change the net effect of tDCS, its intensity and its location (Bestmann et al., 2015; Dayan et al., 2013; Parkin et al., 2015). We do not assume that anodal tDCS necessarily excites the underlying cortical tissue or that cathodal tDCS necessarily inhibits the tissue.

Anisotropy in current flow models has been shown to have significant influence (Gullmar et al., 2010; Haueisen et al., 2002; Windhoff et al., 2013). However, this influence is known to vary strongly across the brain, where in some regions it is negligible while in others it seems important. This variation is relevant at a local scale (single sulcus or gyrus), please see (Gullmar et al., 2010). While we use a very detailed current flow model, our brain activity modeling approach is restricted to 74 areas, collapsing the detailed current flow information of about 30,000 finite elements into one considered brain area. Thus, a representation of anisotropy in the detailed current flow model will likely have a small influence on the outcome of our study. Although deep brain regions were accounted for in the current flow model, they were not considered as elements of the large-scale brain network of neural masses.

For the conducted simulations we chose an absolute value of 4 mV as maximum influence of tDCS, $\hat{u}_{tDCS}$, which was locally scaled according to the current density estimation for each area. The clipping value of 4 mV arises from the polarizing effect of an electric field of 30 V/m as described by (Bikson et al., 2004) considering a mean dendritic length of about 130 μm. Since there is no information about the mean length of the considered neural masses we linearly scaled the influence of tDCS between zero and this maximum value of 4 mV. It was assumed, that the electric field acts on the aligned dendrites of the pyramidal cell

population. Other studies, especially single neuron in vitro studies, restrict the polarization effect to the cell soma and work with maximum polarizations of only 0.2 mV (Reato et al., 2013). The considerably shorter extent of neural matter explains the differing employed voltage values.

In this paper, we used the Pearson correlation coefficient as a standard measure to report functional connectivity (i) in the network of neural masses, and (ii) in the simulated scalp EEG. Despite its known limitations for such recordings as EEG, it is still a widely used measure. Alternatively, measures such as imaginary coherency and phase lag index might be used (for a discussion, see (Stam et al., 2007)).

Conclusions

Stimulation techniques such as transcranial direct current stimulation (tDCS) lead to effects on cognitive processes and positive therapeutic effects on neurological and psychiatric disorders such as depression, pain, or stroke, which outlast the treatment itself. Moreover, variations in functional brain activity at rest have been related to cognitive operations and pathologies. In this study, we demonstrated a link between stimulation and the functional brain organization. tDCS causes a reorganization of functional brain networks by coordinating the competitive interplay of local processes over the entire brain. Thus, our study motivates further modeling studies to test target-oriented activation or suppression of functional sub-networks (e.g. through adapted electrode montages) with the ultimate goal to complement clinical therapy.

Furthermore, we state that the brain is a highly adaptive complex system and tDCS is not a mere polarization technique. Due to the interconnectivity of areas, it is not trivially expectable, what an unsymmetrical activation/inhibition of discrete cortical areas will cause in the dynamic behavior of the network. We showed that both connectivity scaling (interpretable as a synaptic gain) and tDCS are major determinants of dynamic behavior and lead to nontrivial alterations in terms of characteristics of the local temporal model.

The compiled catalog of dynamic network states comprises occurring dynamics specific for the topology of the utilized connectome. We found the structure to be especially important at transitions of network states. Numerous subsequent modeling studies are conceivable, such as providing input into a specific sub-network or re-evaluating network dynamics utilizing a different temporal model and with connectomes from healthy subjects and patients.

Acknowledgments

Appendix A. Supplementary data

Supplementary data to this article can be found online at http://dx.doi.org/10.1016/j.neuroimage.2016.02.015.

References

Antal, A., Varga, E.T., Kincses, T.Z., Nitsche, M.A., Paulus, W., 2004. Oscillatory brain activity and transcranial direct current stimulation in humans. Neuroreport 15, 1307–1310.

Antal, A., Terney, D., Kuhnl, S., Paulus, W., 2010. Anodal transcranial direct current stimulation of the motor cortex ameliorates chronic pain and reduces short intracortical inhibition. J. Pain Symptom Manag. 39, 890–903.

Ardolino, G., Bossi, B., Barbieri, S., Priori, A., 2005. Non-synaptic mechanisms underlie the after-effects of cathodal transcutaneous direct current stimulation of the human brain. J. Physiol. 568, 653–663.

Bachmann, C.G., Muschinsky, S., Nitsche, M.A., Rolke, R., Magerl, W., Treede, R.D., Paulus, W., Happe, S., 2010. Transcranial direct current stimulation of the motor cortex induces distinct changes in thermal and mechanical sensory percepts. Clin. Neurophysiol. 121, 2083–2089.

Bestmann, S., de Berker, A.O., Bonaiuto, J., 2015. Understanding the behavioural consequences of noninvasive brain stimulation. Trends Cogn. Sci. 19, 13–20.

Bikson, M., Inoue, M., Akiyama, H., Deans, J.K., Fox, J.E., Miyakawa, H., Jefferys, J.G., 2004. Effects of uniform extracellular DC electric fields on excitability in rat hippocampal slices in vitro. J. Physiol. 557, 175–190.

Bikson, M., Rahman, A., Datta, A., 2012. Computational models of transcranial direct current stimulation. Clin. EEG Neurosci. 43, 176–183.

Bindman, L.J., Lippold, O.C., Redfearn, J.W., 1964. The action of brief polarizing currents on the cerebral cortex of the rat (1) during current flow and (2) in the production of long-lasting after-effects. J. Physiol. 172, 369–382.

Boggio, P.S., Khoury, L.P., Martins, D.C., Martins, O.E., de Macedo, E.C., Fregni, F., 2009. Temporal cortex direct current stimulation enhances performance on a visual recognition memory task in Alzheimer disease. J. Neurol. Neurosurg. Psychiatry 80, 444–447.

Bota, M., Sporns, O., Swanson, L.W., 2015. Architecture of the cerebral cortical association connectome underlying cognition. Proc. Natl. Acad. Sci. U. S. A. 112, E2093–E2101.

Braitenberg, V., Schuez, A., 1991. Anatomy of the Cortex: Statistics and Geometry. Sprinter, Berlin, New York.

Brunoni, A.R., Nitsche, M.A., Bolognini, N., Bikson, M., Wagner, T., Merabet, L., Edwards, D.J., Valero-Cabre, A., Rotenberg, A., Pascual-Leone, A., Ferrucci, R., Priori, A., Boggio, P.S., Fregni, F., 2012. Clinical research with transcranial direct current stimulation (tDCS): challenges and future directions. Brain Stimul. 5, 175–195.

Contreras, D., 2004. Electrophysiological classes of neocortical neurons. Neural Netw. 17, 633–646.

David, O., Friston, K.J., 2003. A neural mass model for MEG/EEG: coupling and neuronal dynamics. NeuroImage 20, 1743–1755.

Dayan, E., Censor, N., Buch, E.R., Sandrini, M., Cohen, L.G., 2013. Noninvasive brain stimulation: from physiology to network dynamics and back. Nat. Neurosci. 16, 838–844.

Deco, G., Jirsa, V.K., Robinson, P.A., Breakspear, M., Friston, K., 2008. The dynamic brain: from spiking neurons to neural masses and cortical fields. PLoS Comput. Biol. 4, e1000092.

Deco, G., Jirsa, V.K., McIntosh, A.R., 2011. Emerging concepts for the dynamical organization of resting-state activity in the brain. Nat. Rev. Neurosci. 12, 43–56.

Dieckhofer, A., Waberski, T.D., Nitsche, M., Paulus, W., Buchner, H., Gobbele, R., 2006. Transcranial direct current stimulation applied over the somatosensory cortex - differential effect on low and high frequency SEPs. Clin. Neurophysiol. 117, 2221–2227.

Felleman, D.J., Van Essen, D.C., 1991. Distributed hierarchical processing in the primate cerebral cortex. Cereb. Cortex 1, 1–47.

Fornito, A., Zalesky, A., Breakspear, M., 2013. Graph analysis of the human connectome: promise, progress, and pitfalls. NeuroImage 80, 426–444.

Fox, M.D., Buckner, R.L., Liu, H., Chakravarty, M.M., Lozano, A.M., Pascual-Leone, A., 2014. Resting-state networks link invasive and noninvasive brain stimulation across diverse psychiatric and neurological diseases. Proc. Natl. Acad. Sci. U. S. A. 111, E4367–E4375.

Fregni, F., Pascual-Leone, A., 2007. Technology insight: noninvasive brain stimulation in neurology-perspectives on the therapeutic potential of rTMS and tDCS. Nat. Clin. Pract. Neurol. 3, 383–393.

Gibson, E.M., Purger, D., Mount, C.W., Goldstein, A.K., Lin, G.L., Wood, L.S., Inema, I., Miller, S.E., Bieri, G., Zuchero, J.B., Barres, B.A., Woo, P.J., Vogel, H., Monje, M., 2014. Neuronal activity promotes oligodendrogenesis and adaptive myelination in the mammalian brain. Science 344, 1252304.

Gomez Palacio Schjetnan, A., Faraji, J., Metz, G.A., Tatsuno, M., Luczak, A., 2013. Transcranial direct current stimulation in stroke rehabilitation: a review of recent advancements. Stroke Res. Treat. 2013, 170256.

Gullmar, D., Haueisen, J., Reichenbach, J.R., 2010. Influence of anisotropic electrical conductivity in white matter tissue on the EEG/MEG forward and inverse solution. A high-resolution whole head simulation study. NeuroImage 51, 145–163.

Hansen, E.C., Battaglia, D., Spiegler, A., Deco, G., Jirsa, V.K., 2015. Functional connectivity dynamics: modeling the switching behavior of the resting state. NeuroImage 105, 525–535.

Haueisen, J., Tuch, D.S., Ramon, C., Schimpf, P.H., Wedeen, V.J., George, J.S., Belliveau, J.W., 2002. The influence of brain tissue anisotropy on human EEG and MEG. NeuroImage 15, 159–166.

Hummel, F., Cohen, L.G., 2005. Improvement of motor function with noninvasive cortical stimulation in a patient with chronic stroke. Neurorehabil. Neural Repair 19, 14–19.

Jacobson, L., Koslowsky, M., Lavidor, M., 2012. tDCS polarity effects in motor and cognitive domains: a meta-analytical review. Exp. Brain Res. 216, 1–10.

Jansen, B.H., Rit, V.G., 1995. Electroencephalogram and visual evoked potential generation in a mathematical model of coupled cortical columns. Biol. Cybern. 73, 357–366.

Knock, S.A., McIntosh, A.R., Sporns, O., Kotter, R., Hagmann, P., Jirsa, V.K., 2009. The effects of physiologically plausible connectivity structure on local and global dynamics in large scale brain models. J. Neurosci. Methods 183, 86–94.

Kotter, R., 2004. Online retrieval, processing, and visualization of primate connectivity data from the CoCoMac database. Neuroinformatics 2, 127–144.

Kutchko, K.M., Frohlich, F., 2013. Emergence of metastable state dynamics in interconnected cortical networks with propagation delays. PLoS Comput. Biol. 9, e1003304.

Lang, N., Nitsche, M.A., Paulus, W., Rothwell, J.C., Lemon, R.N., 2004. Effects of transcranial direct current stimulation over the human motor cortex on corticospinal and transcallosal excitability. Exp. Brain Res. 156, 439–443.

Liebetanz, D., Nitsche, M.A., Tergau, F., Paulus, W., 2002. Pharmacological approach to the mechanisms of transcranial DC-stimulation-induced after-effects of human motor cortex excitability. Brain 125, 2238–2247.

Lindenberg, R., Renga, V., Zhu, L.L., Nair, D., Schlaug, G., 2010. Bihemispheric brain stimulation facilitates motor recovery in chronic stroke patients. Neurology 75, 2176–2184.

Logothetis, N.K., Murayama, Y., Augath, M., Steffen, T., Werner, J., Oeltermann, A., 2009. How not to study spontaneous activity. NeuroImage 45, 1080–1089.

Lopes da Silva, F., van Rotterdam, A., 1999. Biophysical Aspects of EEG and Magnetoencephalogram Generation. fourth ed.

Luft, C.D., Pereda, E., Banissy, M.J., Bhattacharya, J., 2014. Best of both worlds: promise of combining brain stimulation and brain connectome. Front. Syst. Neurosci. 8, 132.

Mangia, A.L., Pirini, M., Cappello, A., 2014. Transcranial direct current stimulation and power spectral parameters: a tDCS/EEG co-registration study. Front. Hum. Neurosci. 8, 601.

Markram, H., Toledo-Rodriguez, M., Wang, Y., Gupta, A., Silberberg, G., Wu, C., 2004. Interneurons of the neocortical inhibitory system. Nat. Rev. Neurosci. 5, 793–807.

Matsunaga, K., Nitsche, M.A., Tsuji, S., Rothwell, J.C., 2004. Effect of transcranial DC sensorimotor cortex stimulation on somatosensory evoked potentials in humans. Clin. Neurophysiol. 115, 456–460.

Merlet, I., Birot, G., Salvador, R., Molaee-Ardekani, B., Mekonnen, A., Soria-Frish, A., Ruffini, G., Miranda, P.C., Wendling, F., 2013. From oscillatory transcranial current stimulation to scalp EEG changes: a biophysical and physiological modeling study. PLoS One 8, e57330.

Mina, F., Benquet, P., Pasnicu, A., Biraben, A., Wendling, F., 2013. Modulation of epileptic activity by deep brain stimulation: a model-based study of frequency-dependent effects. Front. Comput. Neurosci. 7, 94.

Molaee-Ardekani, B., Marquez-Ruiz, J., Merlet, I., Leal-Campanario, R., Gruart, A., Sanchez-Campusano, R., Birot, G., Ruffini, G., Delgado-Garcia, J.M., Wendling, F., 2013. Effects of transcranial direct current stimulation (tDCS) on cortical activity: a computational modeling study. Brain Stimul. 6, 25–39.

Nitsche, M.A., Paulus, W., 2000. Excitability changes induced in the human motor cortex by weak transcranial direct current stimulation. J. Physiol. 527 (Pt 3), 633–639.

Nitsche, M.A., Roth, A., Kuo, M.F., Fischer, A.K., Liebetanz, D., Lang, N., Tergau, F., Paulus, W., 2007. Timing-dependent modulation of associative plasticity by general network excitability in the human motor cortex. J. Neurosci. 27, 3807–3812.

Nitsche, M.A., Cohen, L.G., Wassermann, E.M., Priori, A., Lang, N., Antal, A., Paulus, W., Hummel, F., Boggio, P.S., Fregni, F., Pascual-Leone, A., 2008. Transcranial direct current stimulation: state of the art 2008. Brain Stimul. 1, 206–223.

Nitsche, M.A., Boggio, P.S., Fregni, F., Pascual-Leone, A., 2009. Treatment of depression with transcranial direct current stimulation (tDCS): a review. Exp. Neurol. 219, 14–19.

Northoff, G., 2012. Immanuel Kant's mind and the brain's resting state. Trends Cogn. Sci. 16, 356–359.

Northoff, G., Qin, P., Nakao, T., 2010. Rest-stimulus interaction in the brain: a review. Trends Neurosci. 33, 277–284.

Nunez, P., 1995. Neocortical Dynamics and Human EEG Rhythms. Oxford University Press, New York.

O'Connell, N.E., Wand, B.M., Marston, L., Spencer, S., Desouza, L.H., 2014. Non-invasive brain stimulation techniques for chronic pain. Cochrane Database Syst. Rev. 4, Cd008208.

Opitz, A., Paulus, W., Will, S., Antunes, A., Thielscher, A., 2015. Determinants of the electric field during transcranial direct current stimulation. NeuroImage 109, 140–150.

Pajevic, S., Basser, P.J., Fields, R.D., 2014. Role of myelin plasticity in oscillations and synchrony of neuronal activity. Neuroscience 276, 135–147.

Parkin, B.L., Ekhtiari, H., Walsh, V.F., 2015. Non-invasive human brain stimulation in cognitive neuroscience: A primer. Neuron 87, 932–945.

Pinotsis, D.A., Moran, R.J., Friston, K.J., 2012. Dynamic causal modeling with neural fields. NeuroImage 59, 1261–1274.

Polania, R., Nitsche, M.A., Paulus, W., 2011a. Modulating functional connectivity patterns and topological functional organization of the human brain with transcranial direct current stimulation. Hum. Brain Mapp. 32, 1236–1249.

Polania, R., Paulus, W., Antal, A., Nitsche, M.A., 2011b. Introducing graph theory to track for neuroplastic alterations in the resting human brain: a transcranial direct current stimulation study. NeuroImage 54, 2287–2296.

Polania, R., Paulus, W., Nitsche, M.A., 2012. Reorganizing the intrinsic functional architecture of the human primary motor cortex during rest with non-invasive cortical stimulation. PLoS One 7, e30971.

Raichle, M.E., 2010. Two views of brain function. Trends Cogn. Sci. 14, 180–190.

Reato, D., Rahman, A., Bikson, M., Parra, L.C., 2010. Low-intensity electrical stimulation affects network dynamics by modulating population rate and spike timing. J. Neurosci. 30, 15067–15079.

Reato, D., Rahman, A., Bikson, M., Parra, L.C., 2013. Effects of weak transcranial alternating current stimulation on brain activity-a review of known mechanisms from animal studies. Front. Hum. Neurosci. 7, 687.

Ruffini, G., Fox, M.D., Ripolles, O., Miranda, P.C., Pascual-Leone, A., 2014. Optimization of multifocal transcranial current stimulation for weighted cortical pattern targeting from realistic modeling of electric fields. NeuroImage 89, 216–225.

Sanz Leon, P., Knock, S.A., Woodman, M.M., Domide, L., Mersmann, J., McIntosh, A.R., Jirsa, V., 2013. The virtual brain: a simulator of primate brain network dynamics. Front. Neuroinform. 7, 10.

Sanz-Leon, P., Knock, S.A., Spiegler, A., Jirsa, V.K., 2015. Mathematical framework for large-scale brain network modeling in the virtual brain. NeuroImage 111, 385–430.

Sehm, B., Schafer, A., Kipping, J., Margulies, D., Conde, V., Taubert, M., Villringer, A., Ragert, P., 2012. Dynamic modulation of intrinsic functional connectivity by transcranial direct current stimulation. J. Neurophysiol. 108, 3253–3263.

Silvanto, J., Muggleton, N., Walsh, V., 2008. State-dependency in brain stimulation studies of perception and cognition. Trends Cogn. Sci. 12, 447–454.

Sotero, R.C., Trujillo-Barreto, N.J., Iturria-Medina, Y., Carbonell, F., Jimenez, J.C., 2007. Realistically coupled neural mass models can generate EEG rhythms. Neural Comput. 19, 478–512.

Spiegler, A., Jirsa, V., 2013. Systematic approximations of neural fields through networks of neural masses in the virtual brain. NeuroImage 83, 704–725.

Spiegler, A., Kiebel, S.J., Atay, F.M., Knosche, T.R., 2010. Bifurcation analysis of neural mass models: impact of extrinsic inputs and dendritic time constants. NeuroImage 52, 1041–1058.

Spiegler, A., Knosche, T.R., Schwab, K., Haueisen, J., Atay, F.M., 2011. Modeling brain resonance phenomena using a neural mass model. PLoS Comput. Biol. 7, e1002298.

Spitoni, G.F., Cimmino, R.L., Bozzacchi, C., Pizzamiglio, L., Di Russo, F., 2013. Modulation of spontaneous alpha brain rhythms using low-intensity transcranial direct-current stimulation. Front. Hum. Neurosci. 7, 529.

Stam, C.J., Nolte, G., Daffertshofer, A., 2007. Phase lag index: assessment of functional connectivity from multi channel EEG and MEG with diminished bias from common sources. Hum. Brain Mapp. 28, 1178–1193.

Thomson, A.M., Bannister, A.P., 2003. Interlaminar connections in the neocortex. Cereb. Cortex 13, 5–14.

Valle, A., Roizenblatt, S., Botte, S., Zaghi, S., Riberto, M., Tufik, S., Boggio, P.S., Fregni, F., 2009. Efficacy of anodal transcranial direct current stimulation (tDCS) for the treatment of fibromyalgia: results of a randomized, sham-controlled longitudinal clinical trial. J. Pain Manag. 2, 353–361.

Van Essen, D.C., Smith, S.M., Barch, D.M., Behrens, T.E., Yacoub, E., Ugurbil, K., 2013. The WU-Minn Human Connectome Project: an overview. NeuroImage 80, 62–79.

Wagner, T., Valero-Cabre, A., Pascual-Leone, A., 2007. Noninvasive human brain stimulation. Annu. Rev. Biomed. Eng. 9, 527–565.

Wagner, S., Rampersad, S.M., Aydin, U., Vorwerk, J., Oostendorp, T.F., Neuling, T., Herrmann, C.S., Stegeman, D.F., Wolters, C.H., 2014. Investigation of tDCS volume conduction effects in a highly realistic head model. J. Neural Eng. 11, 016002.

Wendling, F., Bartolomei, F., Bellanger, J.J., Chauvel, P., 2002. Epileptic fast activity can be explained by a model of impaired GABAergic dendritic inhibition. Eur. J. Neurosci. 15, 1499–1508.

Windhoff, M., Opitz, A., Thielscher, A., 2013. Electric field calculations in brain stimulation based on finite elements: an optimized processing pipeline for the generation and usage of accurate individual head models. Hum. Brain Mapp. 34, 923–935.

Wokke, M.E., Talsma, L.J., Vissers, M.E., 2014. Biasing neural network dynamics using non-invasive brain stimulation. Front. Syst. Neurosci. 8, 246.

Zaghi, S., Heine, N., Fregni, F., 2009. Brain stimulation for the treatment of pain: A review of costs, clinical effects, and mechanisms of treatment for three different central neuromodulatory approaches. J. Pain Manag. 2, 339–352.

Zhang, D., Raichle, M.E., 2010. Disease and the brain's dark energy. Nat. Rev. Neurol. 6, 15–28.